

# ELECTROCHEMISTRY

Milan Skocic, PhD.



$\epsilon$ lectrochemistry  $X$ pertise  $e$ orrosion



# Contents

<b>I</b>	<b>Electrochemical Impedance</b>	<b>1</b>
<b>1</b>	<b>Theory</b>	<b>3</b>
<b>II</b>	<b>PhotoElectrochemistry</b>	<b>5</b>
<b>2</b>	<b>Theory</b>	<b>7</b>
2.1	Introduction . . . . .	7
2.2	Basics . . . . .	7
2.2.1	Electronic Band Structure . . . . .	7
2.2.2	Semiconductor/electrolyte interface in dark condition . . . . .	9
2.2.3	Semiconductor/electrolyte interface under illumination . . . . .	12
2.3	Application Examples . . . . .	13
2.3.1	Identification of minor oxides . . . . .	13
2.3.2	Identification of semiconduction type . . . . .	14
2.3.3	High temperature PEC . . . . .	14
<b>3</b>	<b>Fitting</b>	<b>17</b>
3.1	Introduction . . . . .	17
3.2	Fitting procedure . . . . .	17
3.3	Estimation of the confidence intervals . . . . .	18
3.3.1	Ideal Situation . . . . .	18
3.3.2	Real Situation . . . . .	19
3.4	Application . . . . .	20
3.4.1	Numerically generated energy photocurrent spectra . . . . .	20
3.4.2	Experimental energy photocurrent spectra . . . . .	23
3.5	Conclusion . . . . .	24



# List of Figures

2.1	Schematic representation of the electronic band structure [1]: a) conductor, b) semiconductor, c) isolator . . . . .	8
2.2	Schematic representation of the mechanisms generating charge carriers in semiconductors [2]: a) thermal excitation, b) photoexcitation, c) doping . . . . .	9
2.3	Schematic representation of the Fermi level with respect to the semiconduction type [2]: a) intrinsic, b) n-type, c) p-type. . . . .	9
2.4	Potential gradient at semiconductor/electrolyte interface [3]. $\Phi_{sc}$ and $\Phi_{el}$ correspond to the potentials of the semiconductor and the electrolyte, respectively. $\Delta\Phi_{sc/el}$ corresponds to the potential difference between the semiconductor and the electrolyte. $w_{sc}$ and $w_H$ correspond to the widths of the space charge and the electrical double layer, respectively. . . . .	10
2.5	Schematic representation of the space charge in depletion of majority charge carriers for a semiconductor in contact with an electrolyte [4, 5]: a) n-type, b) p-type. . . . .	10
2.6	Schematic representation of the band bending in p-type and n-type semiconductors in contact with an electrolyte [4, 5]: a) $U = U_{fb}$ , b) $U > U_{fb}$ , c) $U < U_{fb}$ . . . . .	11
2.7	Schematic representation of the mechanism generating a photocurrent [4, 5]. . . . .	12
2.8	Photocurrent density $i_{ph}$ and dark current density $i_d$ with respect to the potential in a case of GaAs semiconductor [6]: a) n-type, b) p-type. . . . .	12
2.9	Photocurrent spectra measured on zirconia oxide layer formed on Zircaloy4 and “pure” zirconium oxidized for 1h at 470°C in oxygenated atmosphere[7]: a) complete spectrum b) close-up view on the minor contributions. . . . .	14
2.10	Photocurrent with respect to the potential for an Ni-based alloy 600 polished and oxidized in simulated PWR for 500 h [8]: a) $P_{H_2}=6.5$ bar, b) $P_{H_2}=0.05$ bar. . . . .	14
2.11	a) Schematic representation of the metallic cell developed by Bojinov et al. [9]. b) Photocurrent spectra performed on iron oxides at different temperatures (up to 200°C) obtained by Bojinov et al. [9]. . . . .	15
2.12	a) Schematic view of the photoelectrochemical cell developed by Skocic [10]. b) Photocurrent energy spectra of an X750 specimen recorded at room temperature and in 280°C/80 bar water [10] . . . . .	15
3.1	Energy photocurrent spectra generated with different amplification factors $f_a$ . . . . .	22
3.2	Energy photocurrent spectra recorded at different potentials on a Ni-based alloy 600 thermally oxidized (experimental data were provided by Petit et al. [11]) . . . . .	23
3.3	Energy photocurrent spectra recorded at different applied potentials on a Ni-based alloy A600 oxidized at 900°C in oxygen for 2h (according to [12]). . . . .	24



# List of Tables

3.1	Parameter values obtained by Petit et al. [11] (figure 1) by numerical fitting. . . . .	20
3.2	Parameters values obtained after numerical fitting of the energy photocurrent spectra generated with different amplification factors ( $f_a$ ). . . . .	21
3.3	Bandgap values and the associated confidence intervals obtained after numerical fitting of the energy photocurrent spectra of the figure 3.1a. . . . .	21
3.4	Parameters values and the associated confidence intervals obtained after numerical fitting of the energy photocurrent spectra of the figure 3.2. The potential is referred with respect to mercury sulfate electrode (MSE, +650 V vs. SHE). . . . .	23
3.5	Parameters values and the associated confidence intervals obtained after numerical fitting of the energy photocurrent spectra of the figure 3.3 . . . . .	24





# Nomenclature

## Acronyms

PEC	PhotoElectroChimie
SHE	Standard Hydrogen Electrode
SCE	Saturated Calomel Electrode
MSE	Mercury Sulphate Electrode
OCV	Open Circuit Voltage
ZRA	Zero Resistance Ammeter
PEEK	PolyEtherEtherKetone
PTFE	PolyTetraFluoroEthylene
ppm	Parts Per Million (rapport massique)
ppb	Parts Per Billion (rapport massique)

## Physical Constants

$h$	Constante de Planck
$c$	Vitesse de la lumière dans le vide
$F$	Constante de Faraday
$R$	Constante universelle des gaz parfaits
$k$	Constante de Boltzmann
$\epsilon_0$	Permittivité du vide
$e$	Charge élémentaire

## Electrochemistry

$\alpha_a$	Coefficient de transfert anodique
$\alpha_c$	Coefficient de transfert cathodique
$b_a$	Pente de Tafel pour la branche anodique
$b_c$	Pente de Tafel pour la branche cathodique
$z$	Nombre d'électrons échangés
$j$	Densité de courant
$j_0$	Densité de courant d'échange

$U$	Potentiel électrochimique, mesuré ou appliqué, par rapport à une référence
$U_{eq}$	Potentiel électrochimique à l'équilibre mesuré par rapport à une référence
$U_{fb}$	Potentiel de bande plate par rapport à une référence
$\eta$	Surtension ( $U - U_{eq}$ )

### Photoelectrochemistry

$\Phi_{sc}$	Potentiel électrique dans le semiconducteur
$\Phi_{el}$	Potentiel électrique dans l'électrolyte
$\epsilon$	Permittivité diélectrique relative
$w_{sc}$	Epaisseur de la charge d'espace
$w_H$	Epaisseur de la double couche électrochimique
$L_{cc}$	Longueur de diffusion moyenne des porteurs de charge minoritaires
$\lambda$	Longueur d'onde de la lumière
$\nu$	Fréquence de la lumière
$h\nu$ ou $E$	Energie de la lumière
$\alpha_{sc}$	Coefficient d'absorption du semiconducteur
$\phi$	Flux de photon
$I_{ph}$	Photocourant tel que mesuré (valeur complexe)
$I_{ph}^*$	Photocourant rapporté à un flux de photons normalisé (valeur complexe)
$\theta$	Phase entre le signal mesuré et le signal de référence correspondant au retard de l'établissement du photocourant par rapport à l'illumination
$K$	facteur d'amplitude du photocourant correspondant à la pente de la transformée linéaire ( $ I_{ph}^*  \cdot  h\nu ^{1/2} = f(h\nu - E_g)$ (loi de Gärtner-Butler)
$E_g$	Largeur de bande interdite (gap)
$E_F$	Niveau de Fermi
$E_c$	Niveau d'énergie correspondant au bas de la bande de conduction
$E_{cs}$	Niveau d'énergie correspondant au bas de la bande de conduction en surface
$E_v$	Niveau d'énergie correspondant au haut de la bande de valence
$E_{vs}$	Niveau d'énergie correspondant au haut de la bande de valence en surface
$E_d$	Niveau d'énergie donneur dans le cas d'un dopage de type $n$
$E_a$	Niveau d'énergie accepteur dans le cas d'un dopage de type $p$
$E_{fb}$	Niveau de Fermi en situation de bandes plates

## Part I

# Electrochemical Impedance



# Chapter 1

## Theory



Part II

PhotoElectrochemistry





# Chapter 2

## Theory

### 2.1 Introduction

In the course of the last 30 years, photoelectrochemical techniques have been shown to be useful tools for characterizing oxidation layers. Interdisciplinary theoretical underpinnings were built [13–17] such as the Gärtner-Butler model [18, 19] which has been proven to be a simple and robust model for the photocurrent generation. Technical progresses were achieved, allowing to study oxide layers at macroscopic, mesoscopic, and microscopic scales [7, 20], or in-situ in high temperature corrosion conditions [9, 10].

First, this paper presents the theoretical background on which the photoelectrochemical techniques rely on. Examples of application are also presented in a second part.

### 2.2 Basics

PEC takes advantage of the photovoltaic effect, discovered by Becquerel [21] in 1839, that occurs at the interface of a semiconductor and an electrolyte. In fact, the first experience showed the occurrence of a photopotential and a photocurrent under illumination when a silver electrode, covered with an oxide layer, was immersed in an acidic medium and connected to a platinum electrode. Nonetheless, the first studies focused on the understanding of the interfacial processes were performed much later [15, 22, 23].

The basics of photoelectrochemistry and application examples are presented in the following sections and they are largely described in the literature [3–5, 13, 24, 25]. Several hypotheses are needed in order to apply the theoretical concepts:

- semiconductor are considered to be ideal i.e. crystallized and homogeneous
- the dielectric constant of the semiconductor is independent of the light wavelength
- the capacity of the Helmholtz layer is greater than the capacitance of the space charge capacitance
- the potential drop in the Helmholtz layer is independent of the applied potential and is negligible

The hypotheses are rarely fully respected in the case of oxides or passive films formed on industrial alloys. Nonetheless, the literature shows that the developed models can be applied to non-ideal systems such as oxides and passive films.

#### 2.2.1 Electronic Band Structure

Solids are generally classified into three groups: conductors, semiconductors and isolators. Each category can be illustrated with a specific band structure as shown in figure 2.1. Valence and conduction bands correspond to allowed energy states for the electrons. The lowest energy level of the conduction band is labeled  $E_c$  and the highest energy level of the valence band is labeled  $E_v$ . They are separated by a band gap,  $E_g$ , with no allowed energy states. The repartition of the electrons among both bands are

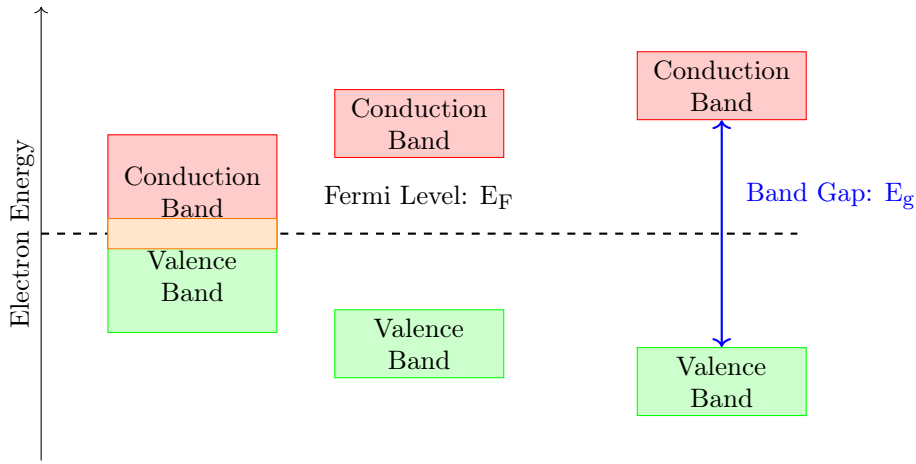


Figure 2.1: Schematic representation of the electronic band structure [1]: a) conductor, b) semiconductor, c) isolator

described by the position of the Fermi Level,  $E_F$ , which represents the highest energy state that can be occupied level at 0K. It is equivalent to the electrochemical potential in solid phases.

The electronic conduction is due to the movement either of the negatively charged electrons in the conduction band or of the positively charged holes in the valence band or both simultaneously. Consequently, the conduction depends on the number of available charge carriers in the conduction band and in the valence band. In conductors, an overlap of the conduction and the valence bands occurs which means that the highest allowed energy band is partially filled. The distinction between a semiconductor and an insulator is less obvious because the conduction depends on the band gap and the energy provided by the environment to the electrons from the valence band in order to jump into the conduction band.

In semiconductors, charge carriers can be generated by three mechanisms: *thermal excitation*, *photoexcitation* and *doping* as shown in figure 2.2. , In the case of very low band gaps, thermal excitation can be enough in order to eject an electron from the valence band to the conduction band. Photoexcitation ejects electrons from the valence band to the conduction band when an incident photon, with energy greater than the band gap, is absorbed. Doping introduces additional energy level located in between the conduction and valence bands.

Doping occurs when the stoichiometry is altered or when impurities are introduced in the crystallographic lattice of the semiconductor. In the case of n-type semiconductors, the donor energy levels  $E_d$  lie just under the conduction band. The electrons from the donor levels are ejected by thermal excitation. Consequently, the majority charge carriers are negatively charged electrons in the band conduction. Similarly, the acceptor energy levels  $E_a$ , of p-type semiconductors, lie just above the band valence. The latter trap electrons from the valence band and therefore create holes. Consequently, the majority charge carriers are positively charged holes.

The Fermi level  $E_F$  in intrinsic semiconductors is located at the mid-gap . The n-type and p-type doping shift the Fermi level towards band edges  $E_c$  and  $E_v$ , respectively. The figure 2.3 shows the position of the Fermi level with respect to the semiconductor type.

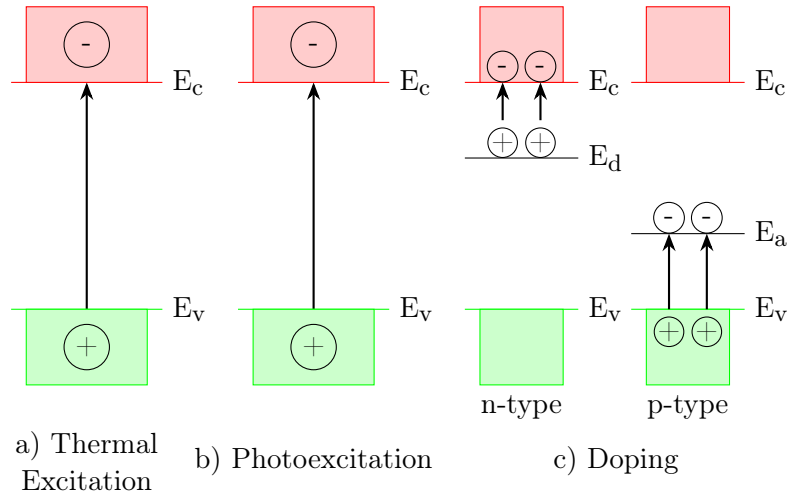


Figure 2.2: Schematic representation of the mechanisms generating charge carriers in semiconductors [2]: a) thermal excitation, b) photoexcitation, c) doping

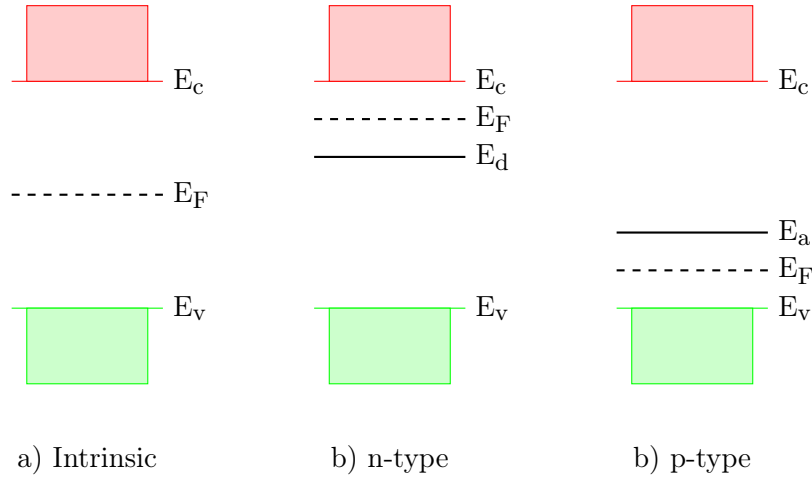


Figure 2.3: Schematic representation of the Fermi level with respect to the semiconduction type [2]: a) intrinsic, b) n-type, c) p-type.

### 2.2.2 Semiconductor/electrolyte interface in dark condition

A potential gradient occurs when a semiconductor comes into contact with an electrolyte as shown in figure 2.4. The position of the Fermi level in the electrolyte with respect to the conduction and valence band edges leads to three different situations after a transient charge transfer. The flat band situation occurs when the Fermi level in the electrolyte matches the Fermi level in the semiconductor. Consequently, there is no potential gradient in the semiconductor. In a case of Fermi level mismatch, a band bending occurs in the semiconductor near the semiconductor/electrolyte interface. The band bending leads to either depletion or accumulation of majority charge carriers near the semiconductor/electrolyte interface. The spatial extension of the depletion/accumulation zone is called space charge as shown in figure 2.5.

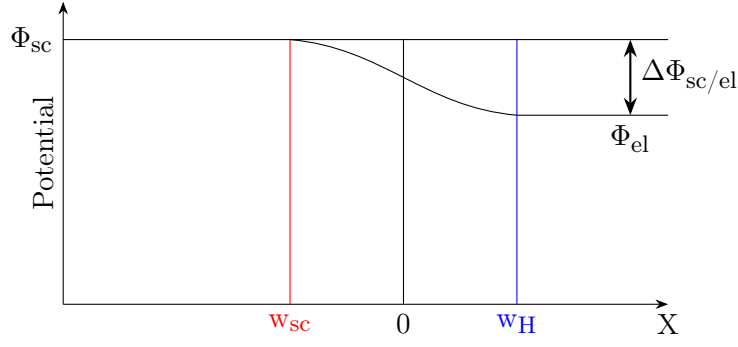


Figure 2.4: Potential gradient at semiconductor/electrolyte interface [3].  $\Phi_{sc}$  and  $\Phi_{el}$  correspond to the potentials of the semiconductor and the electrolyte, respectively.  $\Delta\Phi_{sc/el}$  corresponds to the potential difference between the semiconductor and the electrolyte.  $w_{sc}$  and  $w_H$  correspond to the widths of the space charge and the electrical double layer, respectively.

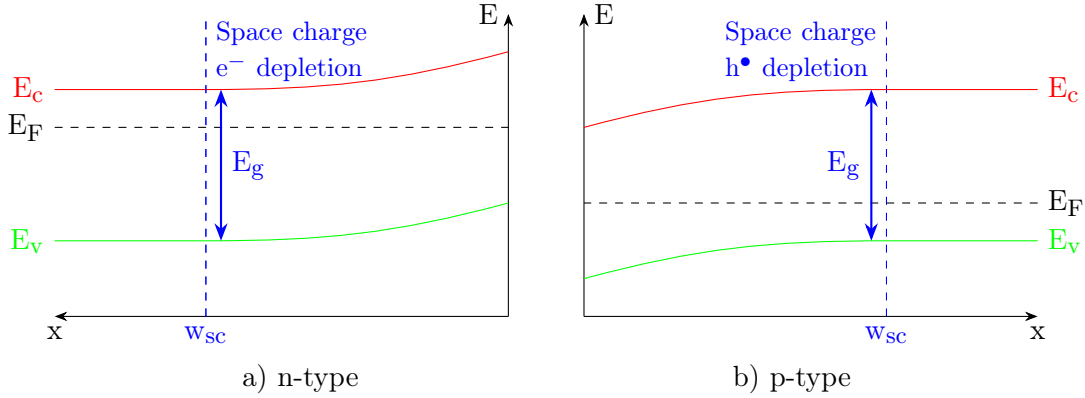


Figure 2.5: Schematic representation of the space charge in depletion of majority charge carriers for a semiconductor in contact with an electrolyte [4, 5]: a) n-type, b) p-type.

Depletion and accumulation as well as band bending can be obtained by polarizing the semiconductor.

As long as the hypothesis described in the introduction paragraph stand, the polarization does not modify the surface band edges  $E_{cs}$  and  $E_{vs}$ . Consequently, the polarization will only alter the band bending in the space charge. Depending on the applied potential,  $U$ , with respect to the flat band potential,  $U_{fb}$ , three different situations will occur as shown in figure 2.6:

- $U = U_{fb}$ : flat band situation no matter the semiconductor type
- $U > U_{fb}$ : depletion (accumulation) in a case of n-type (p-type) semiconductor
- $U < U_{fb}$ : accumulation (depletion) in a case of n-type (p-type) semiconductor

Without illumination, cathodic (anodic) currents are favored in a case of accumulation of electrons (holes) for an n-type (p-type) semiconductor. In fact, the majority charge carriers of n-type (p-type) semiconductors are electrons (holes). Reciprocally, anodic (cathodic) currents are not favored in a case of depletion of electrons (holes) for an n-type (p-type) semiconductor. The junction between a semiconductor and an electrolyte acts like a Schottky diode.

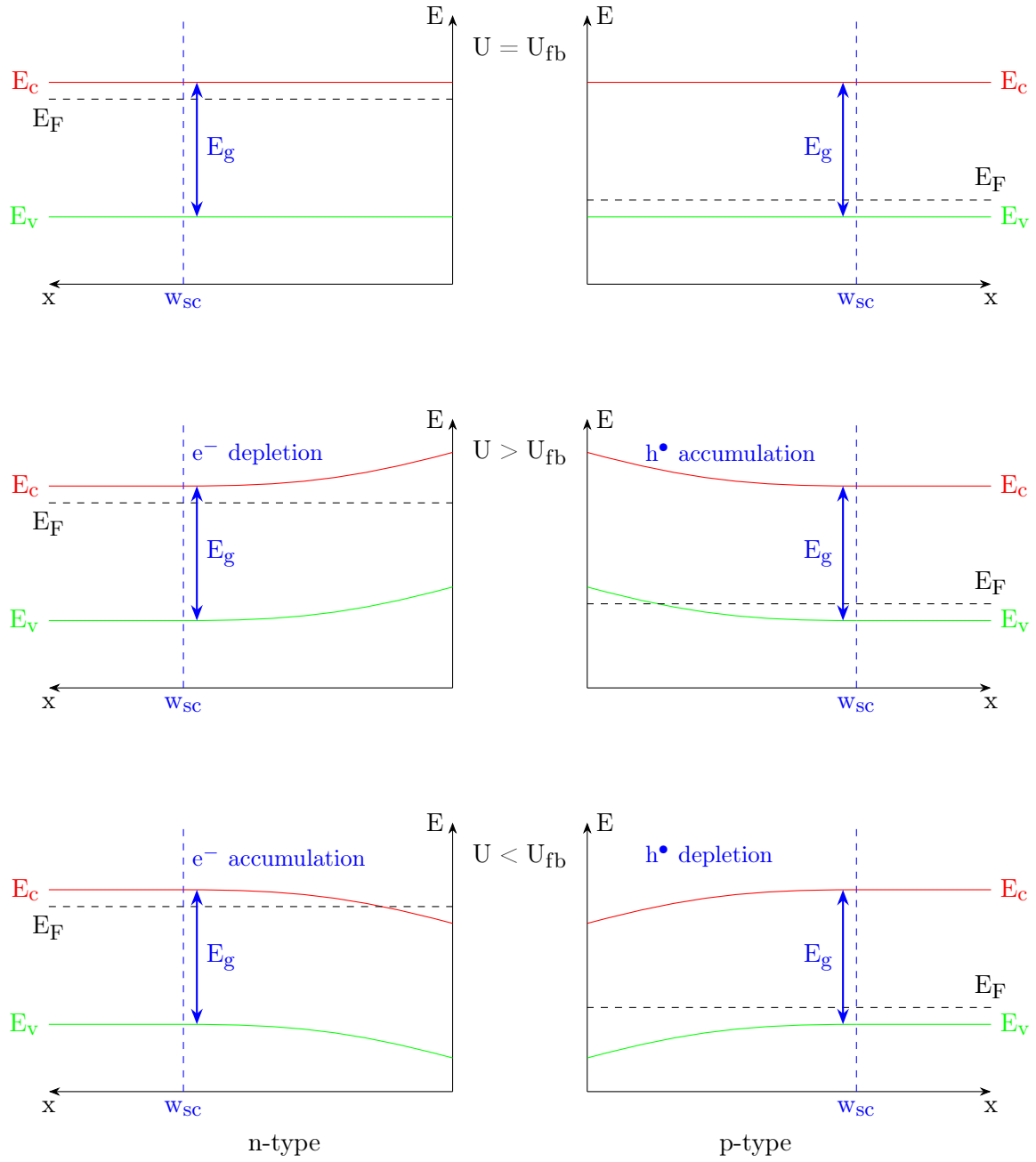


Figure 2.6: Schematic representation of the band bending in p-type and n-type semiconductors in contact with an electrolyte [4, 5]: a)  $U = U_{fb}$ , b)  $U > U_{fb}$ , c)  $U < U_{fb}$ .

### 2.2.3 Semiconductor/electrolyte interface under illumination

The illumination of the semiconductor/electrolyte interface, with photons having an energy greater than the band gap,  $E_g$ , creates electron/hole pairs in the semiconductor. By applying the adequate potential the pairs can be separated. As a consequence, the majority charge carriers are attracted to the semiconductor bulk whereas the minority charge carriers are drawn to the semiconductor/electrolyte interface where they can be transferred to a RedOx species creating an additional current called photocurrent.

Figure 2.7 illustrates schematically the mechanism leading to the creation of a photocurrent. n-type (p-type) semiconductors generate anodic (cathodic) photocurrents where the electrons (holes) move towards the external circuit whereas the holes (electrons) move towards the interface. The photocurrent is significant when the semiconductor/electrolyte junction is in depletion. Figure 2.8 shows the anodic (cathodic) photocurrent for a GaAs n-type (p-type) semiconductor.

Therefore, the applied potential on n-type (p-type) semiconductors is greater (lower) than the flat band potential.

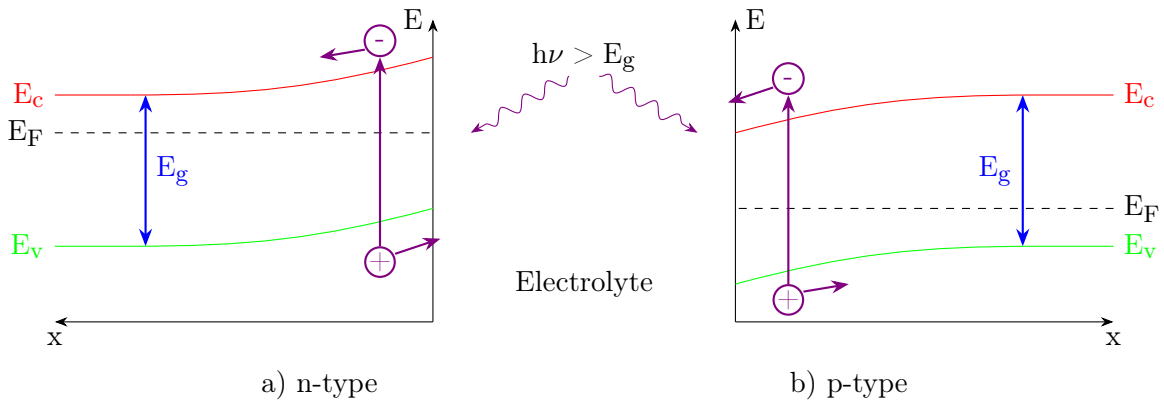


Figure 2.7: Schematic representation of the mechanism generating a photocurrent [4, 5].

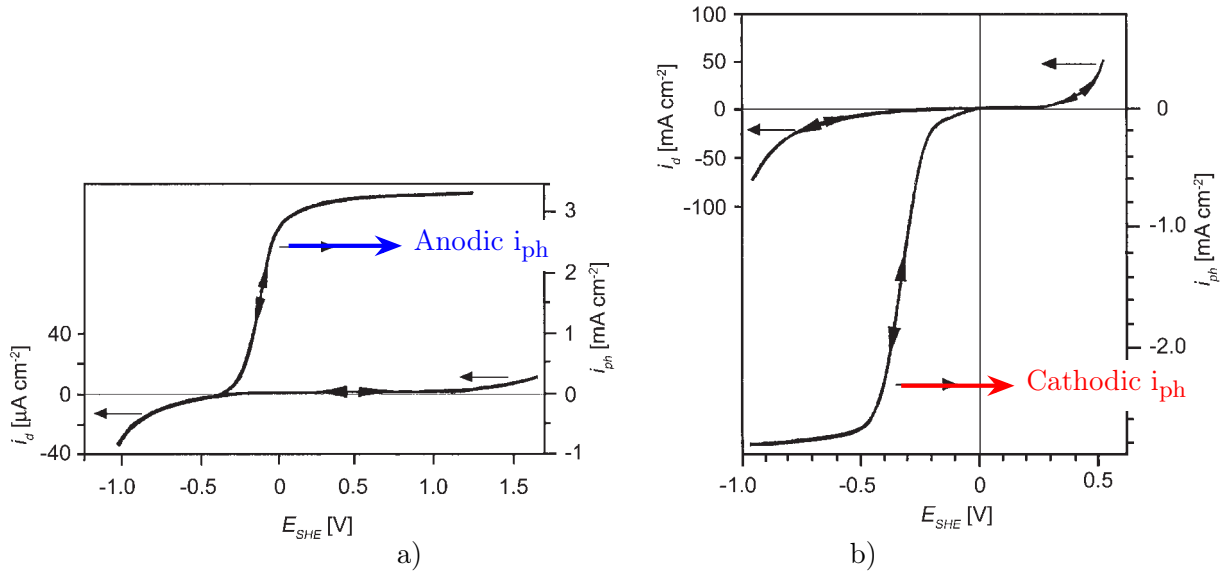


Figure 2.8: Photocurrent density  $i_{ph}$  and dark current density  $i_d$  with respect to the potential in a case of GaAs semiconductor [6]: a) n-type, b) p-type.

Gärtner [18] and Butler [19] proposed a simple and robust model for describing the photocurrent considering that the recombination of the photogenerated electron/hole pairs does not occur in the space charge. Therefore, the photocurrent is proportional to the photon flux  $\Phi_0$ . Moreover, the photocurrent depends on the relative ratio between the space charge width,  $w_{sc}$ , the depth of photon penetration

given by the inverse of the absorption coefficient,  $\alpha$ , and the average diffusion length,  $L_{cc}$ , of the minority charge carriers. In other words, all absorbed photons generate electron/hole pairs and the minority charge carriers are transferred to the electrolyte and therefore contribute to the photocurrent whose expression is given by the equation 2.1.

$$I_{ph} = \phi_0 \left[ 1 - \frac{\exp(-\alpha_{sc} \cdot w_{sc})}{1 + \alpha_{sc} \cdot L_{cc}} \right] \quad (2.1)$$

When  $\alpha_{sc} \cdot w_{sc} \ll 1$  and  $\alpha \cdot L_{cc} \ll 1$ , the photocurrent is approximated by the equation 2.2.

$$I_{ph} = \phi_0 \cdot \alpha \cdot w_{sc} \quad (2.2)$$

The expression of the space charge width,  $w_{sc}$ , in depletion is given by the equation 2.3 according to the Mott-Schottky theory.  $N_{cc}$  represents the number of majority charge carriers, supposed to be equal to the doping,  $e$  corresponds to the elementary charge of an electron.,  $U$  represents the applied potential,  $U_{fb}$  represent the flat band potential,  $\epsilon$  and  $\epsilon_0$  represent the relative and the vacuum permittivity, respectively.

$$w_{sc} = \sqrt{\frac{2\epsilon\epsilon_0}{eN_{cc}} \left( U - U_{fb} - \frac{kT}{e} \right)} \quad (2.3)$$

The expression of the absorption coefficient  $\alpha_{sc}$  with respect to the light energy  $h\nu$  is shown in equation 2.4. The value of  $n$  depends on the band-band transition type.  $n$  takes discrete values of 0.5 or 2 when direct or indirect transitions are allowed, respectively.

$$\alpha_{sc} = \text{const} \frac{(h\nu - E_g)^n}{h\nu} \quad (2.4)$$

The complete expression of the photocurrent is therefore given by the equation 2.5. The latter is obtained by substituting the absorption coefficient  $\alpha_{sc}$  and the space charge width  $w_{sc}$  from the equation 2.2 by the equations 2.3 and 2.4, respectively.

$$I_{ph} = \phi_0 \cdot \text{const} \frac{(h\nu - E_g)^n}{h\nu} \cdot \sqrt{\frac{2\epsilon\epsilon_0}{eN_{cc}} \left( U - U_{fb} - \frac{kT}{e} \right)} \quad (2.5)$$

The linear transform with respect to the energy of the equation 2.5 is shown in equation 2.6 and it is used for determining the band gaps. The linear transform with respect to the potential is shown in equation 2.7 and it is used for determining the semiconduction type, the flat band potential, and the number of majority charge carrier.

$$\left[ \frac{I_{ph} \cdot h\nu}{\phi_0} \right]^{1/n} = \text{const} \cdot (h\nu - E_g) \quad (2.6)$$

$$I_{ph}^2 = \text{const} \cdot \left( U - U_{fb} - \frac{kT}{e} \right) \quad (2.7)$$

## 2.3 Application Examples

### 2.3.1 Identification of minor oxides

Benaboud et al. [7] showed that the photoelectrochemical characterization is robust for detecting the presence of minor oxides. Alloying elements Fe, Sn and Cr, present in Zircaloy4, form precipitates which can be oxidized and trapped in the zirconia layer during the oxidation process. The oxidized precipitates are therefore minor oxide phases in the zirconia layer. illustrates the photocurrent spectra measured on Zircaloy-4 and “pure” zirconium where the strong photocurrent observed at around 5 eV reveals the major oxide i.e. monoclinic zirconia. The photocurrent at energy lower than 5 eV is not null and reveals the presence of minor oxides even in “pure” zirconium despite the very low concentration of impurities. The slope changes provided an estimation of the band gaps where the author identified the presence of hematite, chromia and a solid solution of  $(Fe_xCr_{1-x})O_3$ . The identification is made based on data available in literature [13].

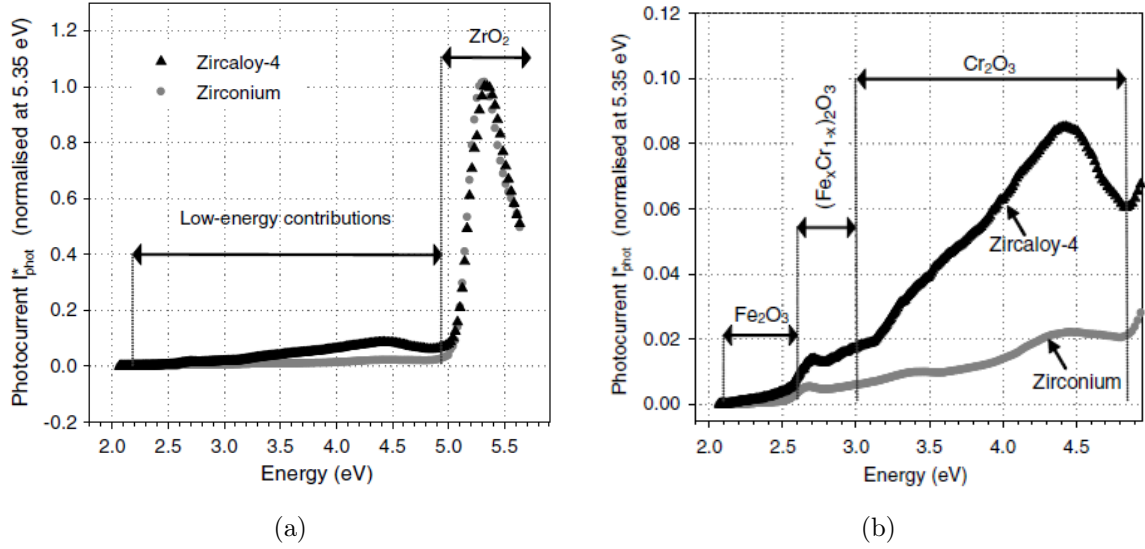


Figure 2.9: Photocurrent spectra measured on zirconia oxide layer formed on Zircaloy4 and “pure” zirconium oxidized for 1h at 470°C in oxygenated atmosphere[7]: a) complete spectrum b) close-up view on the minor contributions.

### 2.3.2 Identification of semiconduction type

Loucif et al. [8] showed the effect of hydrogen pressure on the semiconduction type on Nibased alloy 600 oxidized in simulated PWR. Figure 2.10a shows a “V-shape” of the normalized photocurrent which reveals an isolating behavior of the oxide layer at high hydrogen pressure. Figure 2.10b shows a monotonous increase of the normalized photocurrent towards more anodic potentials which reveals n-type semiconduction.

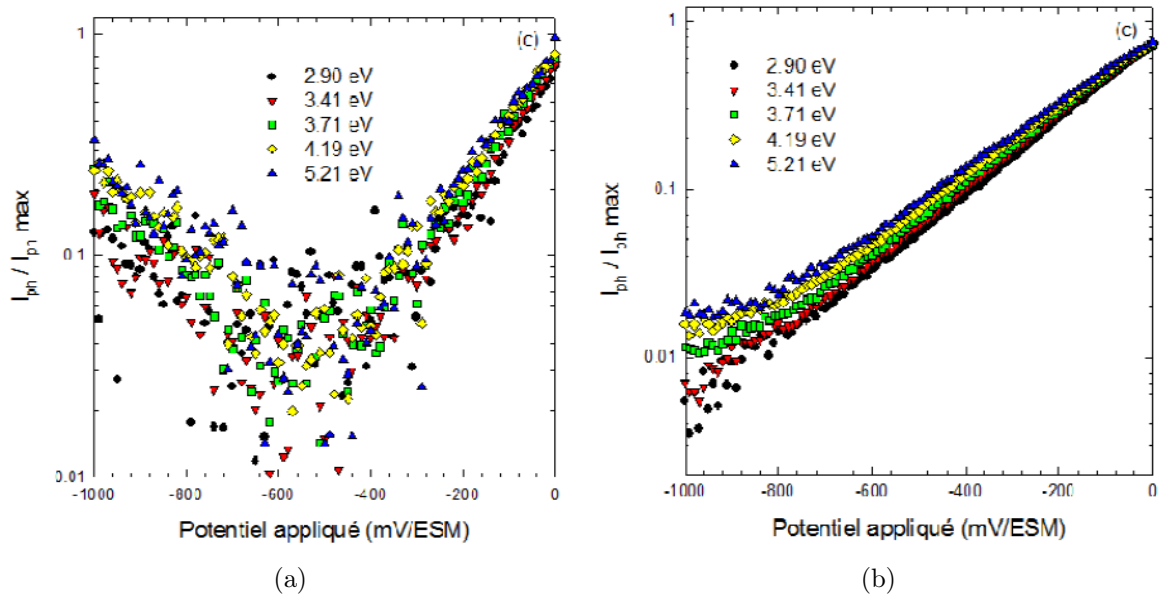


Figure 2.10: Photocurrent with respect to the potential for an Ni-based alloy 600 polished and oxidized in simulated PWR for 500 h [8]: a)  $P_{H_2}=6.5$  bar, b)  $P_{H_2}=0.05$  bar.

### 2.3.3 High temperature PEC

The majority of photoelectrochemical characterizations are performed at room temperature in simple glass/Plexiglas cells where the signal/noise ratio is very good. High temperature photoelectrochemical



characterizations require sophisticated metallic cells and transparent windows able to withstand the arch environment. Despite the need to improve the signal/noise ratio, the feasibility of the in-situ photoelectrochemical characterizations was demonstrated by Bojinov et al. [9] in 2002 and more recently by Skocic [10] in 2015 as shown in figures 2.11 and 2.12.

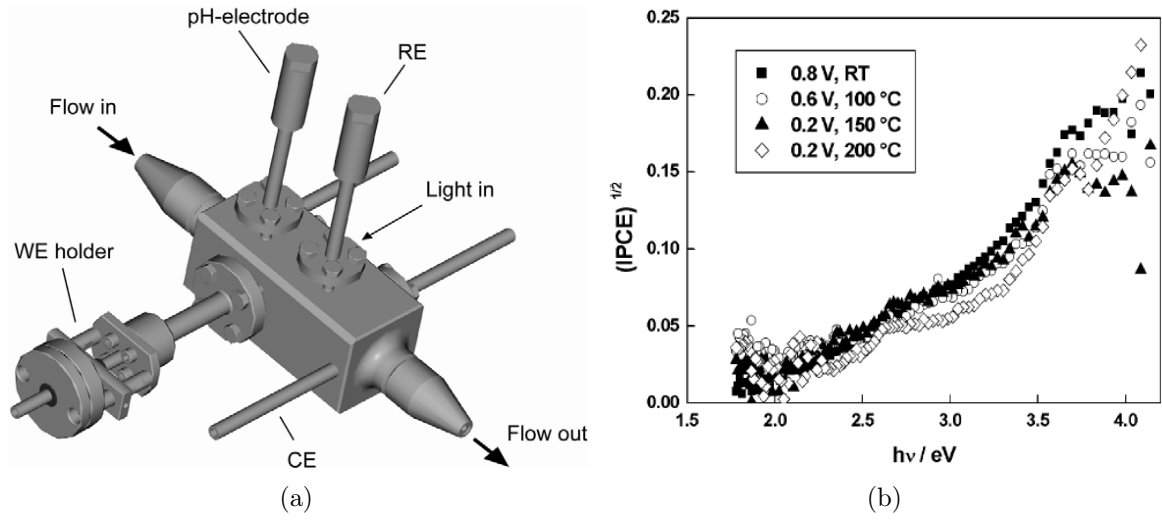


Figure 2.11: a) Schematic representation of the metallic cell developed by Bojinov et al. [9]. b) Photocurrent spectra performed on iron oxides at different temperatures (up to 200°C) obtained by Bojinov et al. [9].

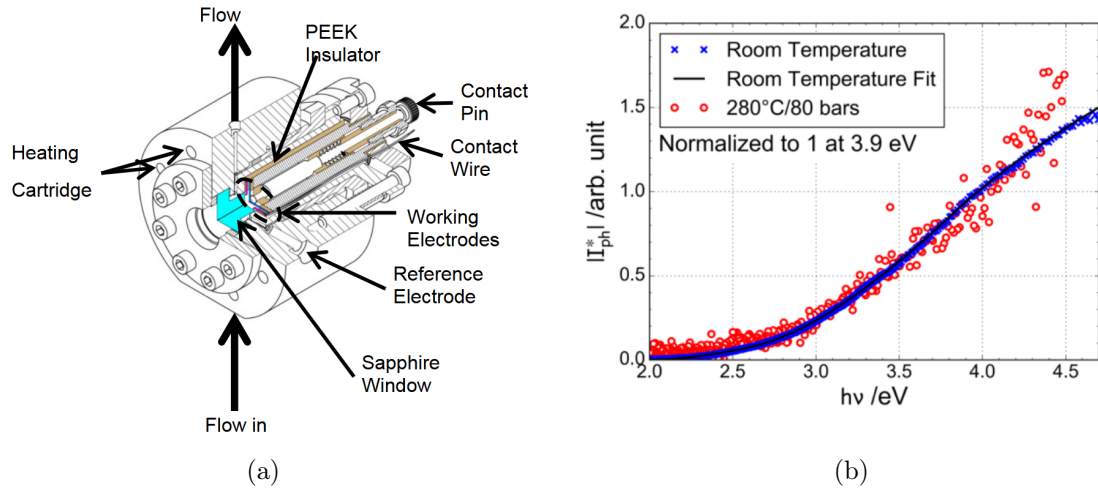


Figure 2.12: a) Schematic view of the photoelectrochemical cell developed by Skocic [10]. b) Photocurrent energy spectra of an X750 specimen recorded at room temperature and in 280°C/80 bar water [10]



# Chapter 3

## Fitting

### 3.1 Introduction

In the course of the last 30 years, photoelectrochemical techniques have been shown to be useful tools for characterizing oxidation layers. Interdisciplinary theoretical underpinnings were built [13–17] such as the Gärtner-Butler model [18, 19] which has been proven to be a simple and robust model for the photocurrent generation. Technical progresses were achieved, allowing to study oxide layers at macroscopic, mesoscopic, and microscopic scales [7, 20], or in-situ in high temperature corrosion conditions [9, 10].

Up to now, for complex oxide scales formed of several p-type and n-type phases, the complete description of the photocurrent energy spectra could not be achieved, and only semi-quantitative and/or partial information could be obtained on the nature of the phases present in the oxide layers. Recently, a new approach was proposed by Petit et al. [11] to analyze the photocurrent spectra which was applied to oxidized duplex stainless steels [9] as well as Ni-based and Zr-based alloys oxidized in LWR conditions [10]. The numerical fitting procedure allowed to obtain high quality fits of the experimental data. Nonetheless, the estimation of the confidence intervals was not implemented.

This paper presents the additional work carried out in order to implement the estimation of the confidence intervals based on the fitting procedure developed by Petit et al. [11]. The latter was rewritten in Python which is an open source interpreted programming language. It is largely used in the scientific community [26–29] and it comes with optimized libraries for numerical computations [30, 31] and a high quality 2D visualization library [32].

### 3.2 Fitting procedure

It should be reminded that the low photocurrents are extracted from the overall electrochemical current using a modulation of the light illuminating the sample. The modulation is obtained with a mechanical chopper placed on the optical path. The reference signal of the modulation is connected to the external reference input of a lock-in amplifier, whereas the current output is connected to the signal input of the latter, allowing to measure both the modulus,  $|I_{ph}|$ , and the phase shift,  $\theta$  of the so called as-measured photocurrent,  $I_{ph}$ . Then, the latter is converted, at each photon energy, in a more useful value,  $I_{ph}^*(h\nu)$ , proportional to the quantum yield of the photocurrent, by dividing  $I_{ph}(h\nu)$  by  $\Phi(h\nu)/\Phi_{max}$ , where  $\Phi(h\nu)$  is the photon flux arriving onto the sample, and  $\Phi_{max}$  its maximum value.

As  $I_{ph}^*$  is measured under modulated light conditions and thus actually was a complex number, it was proposed that the real part  $\Re I_{ph}^*$  and the imaginary part  $\Im I_{ph}^*$  of the photocurrent  $I_{ph}^*$  should be considered simultaneously when analyzing and fitting the photocurrent energy spectra, rather than the modulus  $|I_{ph}^*|$  only, as it was the case up to now. Therefore, the overall complex photocurrent,  $I_{ph}^*$ , was written as shown in eq. 3.1.

$$\begin{aligned}
I_{ph}^* &= |I_{ph}^*| \cdot \cos \theta + |I_{ph}^*| \cdot \sin \theta \\
I_{ph}^* &= \sum_i |I_{ph,i}^*| \cdot \cos \theta_i + \sum_i |I_{ph,i}^*| \cdot \sin \theta_i
\end{aligned} \tag{3.1}$$

where  $|I_{ph,i}^*|$  and  $\theta_i$  represent the modulus and phase shift, respectively, of the photocurrent issued from the  $i^{\text{th}}$  semiconducting constituent of the oxide layer. For thin semiconducting films such as those usually investigated in most corrosion studies, the space charge regions are low compared to penetration depth of the light.  $|I_{ph,i}^*|$  may thus be expected, at a given applied potential, to follow the simplified form of the Gärtner–Butler model, i.e. in fact to obey to the eq. 3.2.

$$\left(|I_{ph,i}^*| \cdot E\right)^{\frac{1}{n}} = K_i \cdot (E - E_{g,i}) \tag{3.2}$$

where  $E_{g,i}$  and  $K_i$  represent the energy gap and a proportionality value, respectively. It should be emphasized that the as-defined  $|I_{ph,i}^*|$  is proportional to, but not equal, to the quantum yield for the  $i$ th semiconducting constituent.  $n$  depends on the band to band transition type,  $n = 1/2$  for an allowed direct transition, and  $n = 2$  for an allowed indirect transition. To our knowledge, the case where  $n = 1/2$  (direct transition) was rarely observed in the case of passive films or more or less disordered thin oxide films.

In addition, as the space charge regions are likely to extend over the whole thickness of each phase in the oxide layer, it is assumed that the recombination of the photogenerated electron–hole pairs, and thus the phase shifts,  $\theta_i$ , will not depend on the photon energy. A given vector of  $m$  ( $E_{g,i}$ ,  $K_i$ ,  $\theta_i$ ) triplets represents the supposed number of semiconducting phases contributing to the photocurrent. The scalar function,  $D$ , to be minimized is given in eq. 3.3 which represents a measurement of the distance between the experimental and calculated data.

$$\left(|I_{ph,i}^*| \cdot E\right)^{\frac{1}{n}} = K_i \cdot (E - E_{g,i}) \tag{3.3}$$

### 3.3 Estimation of the confidence intervals

The scalar function to be minimized defined in 3.3 used for fitting the photocurrent spectra ensures a fairly fast convergence towards the 3m parameters defining the semiconductive contributions. However, the as-defined scalar function could not be used for estimating the confidence intervals. An alternative scalar function was defined to be computed with the optimal parameters in order to estimate the confidence intervals. The statistics of curve fitting shows that the confidence intervals can be estimated using the least-squares method which can be applied to nonlinear systems [33, 34].

The least-squares regression uses the proprieties of the  $\chi^2$  distribution. Consequently, of the experimental measurements of the photocurrent spectra are assumed to follow the normal distribution. Moreover, the least-squares method can be strictly applied only when the experimental variances are known for each energy value of the photocurrent spectrum. Nonetheless, the latter are not always known as it is the case for the photoelectrochemical characterizations. Consequently, modifications of the relationships defined for the ideal situation were necessary.

#### 3.3.1 Ideal Situation

The equation 3.4 presents the scalar function  $\chi^2$  defined in the least-squares method when the experimental variances  $\sigma_{\text{exp}}^2$  are known. The residuals,  $\epsilon$ , weighted by the inverse of variances are given by the equation 3.5.  $\chi^2$  is therefore defined as the sum of the weighted residuals as illustrated by the equation 3.6

$$\chi^2 = \sum_{h\nu} \frac{|I_{\text{ph,calc}} - I_{\text{ph,exp}}|^2}{\sigma_{\text{exp}}^2} \quad (3.4)$$

$$\epsilon = \frac{|I_{\text{ph,calc}} - I_{\text{ph,exp}}|^2}{\sigma_{\text{exp}}} \quad (3.5)$$

$$\chi^2 = \sum_{h\nu} \epsilon^2 \quad (3.6)$$

$\nabla\chi^2$  approaches zero when the parameter values are approaching the optimum values. The covariance matrix of the fitted parameters,  $\sigma_p^2$ , can be estimated with the Jacobian,  $J_\epsilon$ , of the weighted residuals [33] and its expression is given by the equation 3.12. For nonlinear systems, as it is the case for the photocurrent, the equation 3.12 is a first-order approximation. In fact, the approximation is valid because the second-order terms are close to zero which avoids to compute the Hessian [35].

$$\sigma_p = (J_\epsilon^T \cdot J_\epsilon)^{-1} \quad (3.7)$$

The diagonal terms of the covariance matrix represent the variances of the parameters. The P% confidence interval of the parameters,  $CI_{P\%}$  is obtained by multiplying the standard deviations with the student coefficient,  $t_{\text{dof,P}}$ , with dof being the degree of freedom corresponding to number of experimental points of the photocurrent, N, minus the number of parameter, 3m. The probability P% was set to 95%. The confidence intervals of the parameters are given by the equation 3.8.

$$CI_P = \sqrt{\text{diag}(\sigma_p^2)} \cdot t_{\text{dof,P}} \quad (3.8)$$

$$\text{dof} = N - 3m$$

### 3.3.2 Real Situation

The confidence interval can be estimated even when the experimental variances,  $\sigma_{\text{exp}}^2$ , are not known. However, it is necessary to modify the equations presented in section 3.1. The objective is to define a scalar function, S, which behaves like  $\chi^2$  with a constant scaling factor g. The scalar function, S, is defined using real and positive weighting terms, w, as shown in equation 3.6. Similarly to the Equation 6, the S function corresponds to the sum of the weighted residuals  $\epsilon'$ .

$$S = \sum_{h\nu} \frac{|I_{\text{ph,calc}} - I_{\text{ph,exp}}|^2}{w^2} \quad (3.9)$$

The weighting terms are defined in order to isolate the scaling factor, g, and the experimental variances such as illustrated by the equation 3.10. Therefore, the weighting terms are considered proportional to the experimental variances.

$$w = g \cdot \frac{1}{\sigma_{\text{exp}}^2} \quad (3.10)$$

Combining equation 3.9 and equation 3.10, the scalar function S becomes proportional to  $\chi^2$ . Moreover,  $\frac{\chi^2}{\nu}$  goes to unity when the optimum values of the parameters are reached. Consequently, the scaling factor g can be computed with the optimum value of S as shown by the equation 3.11.

$$S = g \cdot \chi^2$$

$$\frac{S}{\nu} = g \cdot \frac{\chi^2}{\nu} \simeq 1 \quad (3.11)$$

The covariance matrix,  $\sigma_p$ , can therefore be estimated with the scaling factor  $g$  and the Jacobian of the weighted residuals,  $J_{e'}$  as illustrated by the equation 3.12. The confidence intervals are then computed using the Equation 3.8.

$$\begin{aligned}\sigma_p'^2 &= (J_{e'}^T \cdot J_{e'})^{-1} \\ \sigma_p &= g \cdot \sigma_p'\end{aligned}\tag{3.12}$$

The choice of the weighted terms was made considering that the experimental variances are proportional to average noise of the photocurrent modulus in dark conditions,  $\bar{\epsilon}_d$ . It has been proposed that the variances are smaller when the quantum yield is greater. The latter is represented by the photocurrent corrected by the photon flux normalized to its maximum value,  $I_{ph,N}$ . The normalization ensures that the weighting terms have the same dimension as the inverse of the variances as shown in equation 3.13.  $S$  is therefore adimensional as it is the case for  $\chi^2$ . The Jacobian,  $J_{e'}$  is numerically estimated by fixing the finite difference step to the squared root of the machine precision [34, 35].

$$\begin{aligned}\sigma_{exp}^2 &\propto \frac{\bar{\epsilon}_d}{|I_{ph,N}|} \\ w &= \frac{1}{\sigma_{exp}^2} = g \cdot \frac{|I_{ph,N}|^2}{\bar{\epsilon}_d^2}\end{aligned}\tag{3.13}$$

## 3.4 Application

### 3.4.1 Numerically generated energy photocurrent spectra

The weighted terms, as previously defined, represent the signal/noise ratio. In order to test the relevancy of the weighted terms, energy photocurrent spectra were recomputed (eq. 3.1) from parameter values obtained by Petit et al. [11] by fitting a fairly simple energy photocurrent spectrum having 3 semiconductive contributions. The values of the parameters are presented in table 3.1.

	$10^5 K_i$ $A^{1/2} \cdot eV^{1/2}$	$\theta_i$ $^\circ$	$E_{g,i}$ eV
	4.6	7.0	1.91
	5.4	-33.0	2.44
	7.0	156.0	3.16

Table 3.1: Parameter values obtained by Petit et al. [11] (figure 1) by numerical fitting.

An increasing noise was added to the computed values of  $I_{ph}$ . The noise was calculated using a normal centered distribution  $N(0, \sigma)$  where  $\sigma$  was set to the minimal value of the calculated photocurrent and then amplified using an amplification factor  $f_a$ . The generated noise was added to real and imaginary parts of the photocurrent  $I_{ph}$ . The modules of the corrected photocurrent  $I_{ph}^*$  for different amplification factors are shown in figure 3.1 and the corresponding values of the fitted parameters are presented in table 3.2. The confidence intervals increased when the signal/noise ratio decreased as it was expected.

The estimation of the confidence intervals can also be helpful for determining the number of semiconductive contribution in an energy photocurrent spectrum. In fact, the determination of the number of semiconductive contributions is an iterative operation by adding contributions until the spectrum is correctly fitted. The estimation of the confidence intervals can be used as a break point of the iterative search when the intervals of two contributions are overlapping i.e. they are no more statistically discernable.

For the sake of illustration, the energy photocurrent of the figure 3.1a was fitted by considering 3, 4 and 5 semiconductive contributions for energies ranging from 1.8 eV to 4.0 eV. Table 3.3 shows the bandgap values and the associated confidence intervals obtained after numerical fitting.

$f_a$	$10^5 K_i$ $A^{1/2} \cdot eV^{1/2}$	$\theta_i$ $^\circ$	$E_{g,i}$ eV
0.0001	$4.6000 \pm 0.0002$	$7.00 \pm 0.02$	$1.9100 \pm 0.0002$
	$5.4000 \pm 0.0004$	$-33.00 \pm 0.02$	$2.4400 \pm 0.0003$
	$7.0000 \pm 0.0009$	$156.00 \pm 0.02$	$3.1600 \pm 0.0009$
1	$4.6 \pm 0.2$	$-7 \pm 4$	$1.91 \pm 0.04$
	$5.5 \pm 0.4$	$-33 \pm 5$	$2.45 \pm 0.08$
	$7.0 \pm 0.3$	$156 \pm 4$	$3.15 \pm 0.04$
2	$4.6 \pm 0.6$	$-7 \pm 7$	$1.91 \pm 0.09$
	$5.5 \pm 0.7$	$-32 \pm 20$	$2.4 \pm 0.2$
	$7.0 \pm 0.5$	$160 \pm 6$	$3.2 \pm 0.2$
5	$5 \pm 3$	$8 \pm 30$	$1.9 \pm 0.4$
	$5 \pm 3$	$-38 \pm 50$	$2.4 \pm 0.5$
	$7 \pm 3$	$154 \pm 20$	$3.2 \pm 0.2$
10	$5 \pm 8$	$10 \pm 80$	$1.9 \pm 0.9$
	$5 \pm 6$	$-43 \pm 200$	$2 \pm 2$
	$6 \pm 4$	$-155 \pm 60$	$3.1 \pm 0.7$

Table 3.2: Parameters values obtained after numerical fitting of the energy photocurrent spectra generated with different amplification factors ( $f_a$ ).

m	3	4	5
$E_{g,1}$	$1.91 \pm 0.07$	$1.9 \pm 0.4$	$1.9 \pm 0.1$
$E_{g,2}$	$2.4 \pm 0.2$	$2 \pm 5$	$2 \pm 4$
$E_{g,3}$	$3.16 \pm 0.06$	$2.5 \pm 0.4$	$2.5 \pm 0.2$
$E_{g,4}$		$3.16 \pm 0.06$	$2.7 \pm 0.2$
$E_{g,5}$			$3.2 \pm 0.1$

Table 3.3: Bandgap values and the associated confidence intervals obtained after numerical fitting of the energy photocurrent spectra of the figure 3.1a.

The numerical fitting, by considering 4 contributions, showed that the contribution with a bandgap value of 1.91 eV was split into two contributions (1.9 eV and 2 eV). The second one featured a confidence interval in the same order of magnitude as the value itself i.e. the 4th contribution did not improve the fitting of the experimental data. The numerical fitting, by considering 5 contributions, showed that the same splitting of the contribution with a bandgap value of 1.91 eV. Moreover, the contribution with a bandgap value of 2.4 eV was split into two contributions (2.6 eV and 2.7 eV) whose confidence intervals were overlapping indicating that they were not statically discernable.

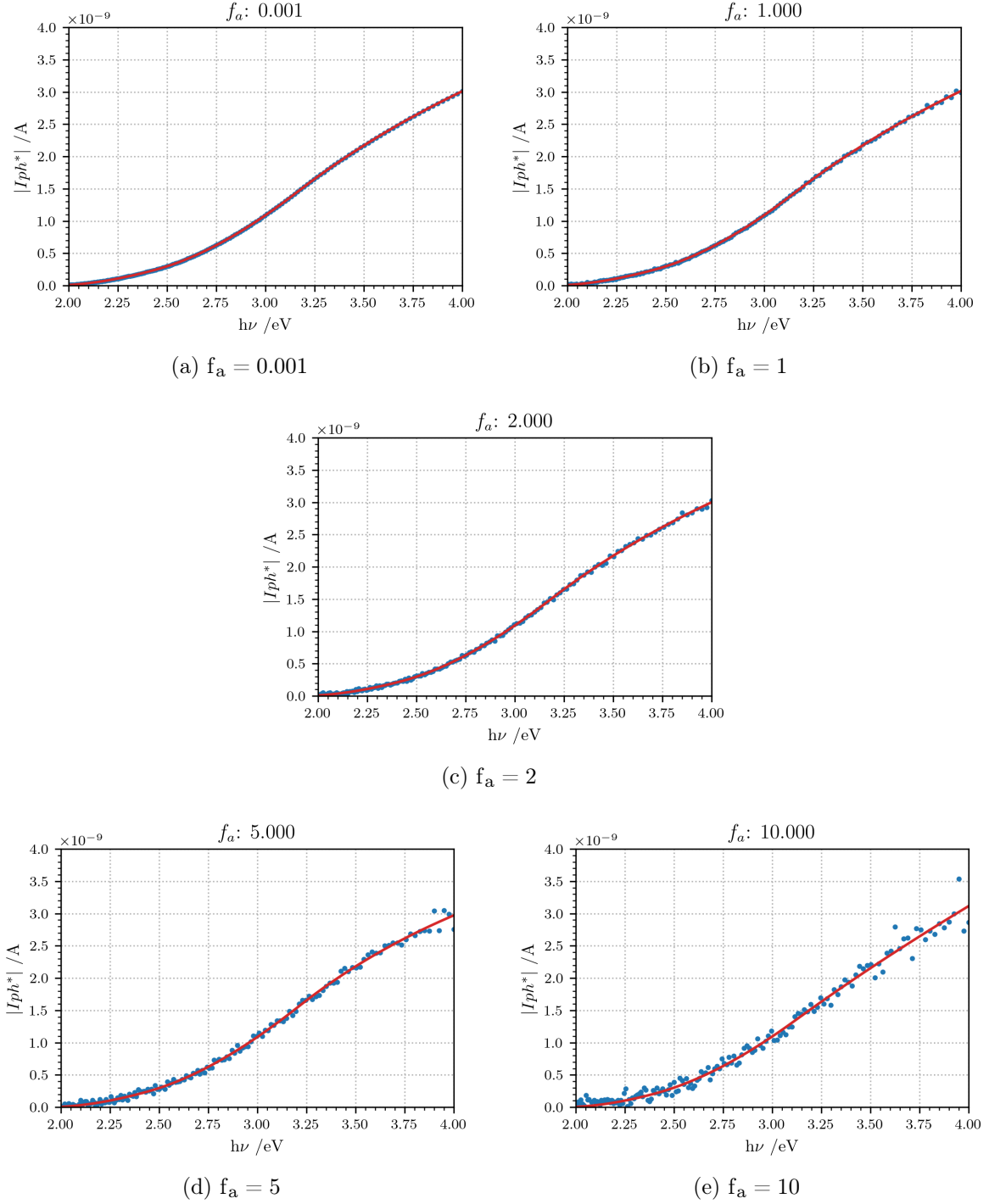


Figure 3.1: Energy photocurrent spectra generated with different amplification factors  $f_a$ .



### 3.4.2 Experimental energy photocurrent spectra

The defined procedure for estimating the interval confidences was then applied to energy photocurrent spectra recorded at different potentials on a Ni-based alloy 600 thermally oxidized. The experimental data were provided by Petit et al. [11]. The experimental, as well as the fitted, modules of the corrected photocurrent  $|I_{ph}^*|$  are illustrated in figure 3.2.

The photocurrent modulus in dark conditions,  $\bar{\epsilon}_d$ , was computed by taking the average of the photocurrent modulus for the five highest energies (6.19, 6.17, 6.14 and 6.08 eV) where the emission spectrum of a Xe lamp can be reasonably considered close to zero. The photocurrent modulus featured a strong decrease for energies lower than 3 eV when the potential decreased towards more cathodic values indicating that the ratio signal/noise decreased as well.

Table 3.4 shows the parameters and the associated confidence intervals obtained after numerical fitting of the experimental data. The increase of the computed confidence intervals for the three first contributions, having bandgap values lower than 3 eV, mirrored correctly the decrease of the ratio signal/noise observed on the experimental data in figure 3.2.

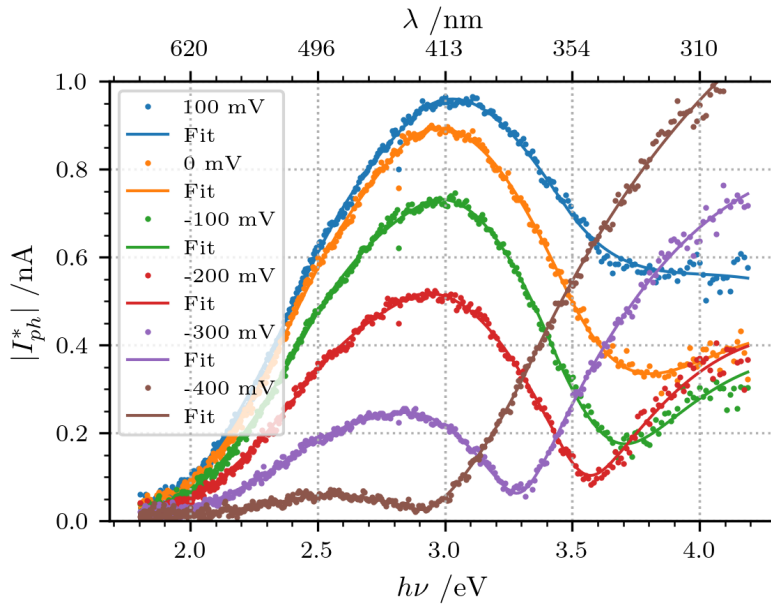


Figure 3.2: Energy photocurrent spectra recorded at different potentials on a Ni-based alloy 600 thermally oxidized (experimental data were provided by Petit et al. [11])

U mV	$10^5 K_i$ $A^{1/2} \cdot eV^{1/2}$	$\theta_i$ °	$E_{g,i}$ eV	$10^5 K_i$ $A^{1/2} \cdot eV^{1/2}$	$\theta_i$ °	$E_{g,i}$ eV	$10^5 K_i$ $A^{1/2} \cdot eV^{1/2}$	$\theta_i$ °	$E_{g,i}$ eV	$10^5 K_i$ $A^{1/2} \cdot eV^{1/2}$	$\theta_i$ °	$E_{g,i}$ eV
100	$5.19 \pm 0.09$	$-42.6 \pm 0.5$	$1.74 \pm 0.02$	$6.4 \pm 0.4$	$122 \pm 2$	$2.42 \pm 0.04$	$6.5 \pm 0.4$	$134 \pm 4$	$2.88 \pm 0.05$	$8.9 \pm 0.8$	$-64 \pm 6$	$3.47 \pm 0.06$
0	$5.14 \pm 0.07$	$-49.2 \pm 0.5$	$1.755 \pm 0.008$	$6.1 \pm 0.3$	$120 \pm 2$	$2.41 \pm 0.04$	$6.8 \pm 0.4$	$131 \pm 4$	$2.82 \pm 0.04$	$9.1 \pm 0.9$	$-58 \pm 6$	$3.48 \pm 0.06$
-100	$4.7 \pm 0.1$	$-52.4 \pm 0.5$	$1.76 \pm 0.02$	$6.1 \pm 0.3$	$119 \pm 2$	$2.44 \pm 0.03$	$6.9 \pm 0.4$	$131 \pm 4$	$2.91 \pm 0.04$	$9.2 \pm 0.9$	$-56 \pm 6$	$3.43 \pm 0.06$
-200	$4.01 \pm 0.06$	$-53.5 \pm 0.6$	$1.76 \pm 0.02$	$5.1 \pm 0.4$	$121 \pm 3$	$2.43 \pm 0.04$	$6.1 \pm 0.4$	$124 \pm 4$	$2.85 \pm 0.04$	$8.3 \pm 0.7$	$-63 \pm 6$	$3.46 \pm 0.06$
-300	$2.9 \pm 0.3$	$-52 \pm 2$	$1.76 \pm 0.05$	$4.2 \pm 0.6$	$122 \pm 5$	$2.42 \pm 0.09$	$5.7 \pm 0.5$	$122 \pm 4$	$2.82 \pm 0.08$	$7.6 \pm 0.3$	$-64 \pm 3$	$3.43 \pm 0.06$
-400	$1 \pm 2$	$-50 \pm 30$	$1.7 \pm 0.6$	$4 \pm 3$	$120 \pm 20$	$2.4 \pm 0.5$	$5 \pm 2$	$130 \pm 20$	$2.8 \pm 0.3$	$6.7 \pm 0.7$	$-61 \pm 6$	$3.35 \pm 0.08$

Table 3.4: Parameters values and the associated confidence intervals obtained after numerical fitting of the energy photocurrent spectra of the figure 3.2. The potential is referred with respect to mercury sulfate electrode (MSE, +650 V vs. SHE).

The fitting procedure was also applied to additional photocurrent spectra obtained by Srisrual [12]

where up to 12 contributions were found to be statistically discernable over 3 different potentials as illustrated in figure 3.3 and table 3.5. Applying the adequate potential, i.e. applying the adequate band bending, the precision on the bang gap values can be enhanced in order to better assess the whole range of band gaps that can occur in an oxide layer.

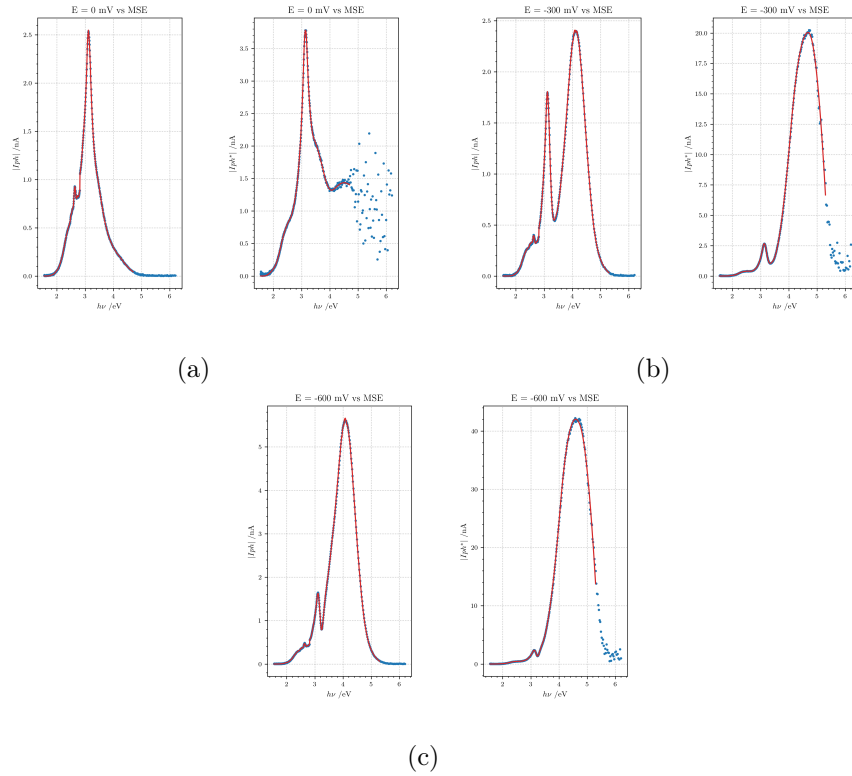


Figure 3.3: Energy photocurrent spectra recorded at different applied potentials on a Ni-based alloy A600 oxidized at 900°C in oxygen for 2h (according to [12]).

	0mV <sub>MSE</sub>	-300mV <sub>MSE</sub>	-600mV <sub>MSE</sub>
E <sub>g,1</sub>	1.7 ± 0.2	2 ± 3	2 ± 20
E <sub>g,2</sub>	2.0 ± 0.2	2 ± 3	2 ± 8
E <sub>g,3</sub>	2.25 ± 0.09	2 ± 1	2 ± 4
E <sub>g,4</sub>	2.58 ± 0.04	2.6 ± 0.3	3 ± 2
E <sub>g,5</sub>	2.8 ± 0.04	2.9 ± 0.2	2.8 ± 0.9
E <sub>g,6</sub>	2.96 ± 0.02	3.08 ± 0.01	3.09 ± 0.05
E <sub>g,7</sub>	3.077 ± 0.0022	3.16 ± 0.03	3.2 ± 0.2
E <sub>g,8</sub>	3.195 ± 0.003	3.19 ± 0.02	3.2 ± 0.05
E <sub>g,9</sub>	3.27 ± 0.02	3.42 ± 0.03	3.42 ± 0.04
E <sub>g,10</sub>	3.44 ± 0.03	4.073 ± 0.009	4.047 ± 0.008
E <sub>g,11</sub>	3.8 ± 0.3	4.7 ± 0.1	4.7 ± 0.2
E <sub>g,12</sub>	4.1 ± 0.5		

Table 3.5: Parameters values and the associated confidence intervals obtained after numerical fitting of the energy photocurrent spectra of the figure 3.3

### 3.5 Conclusion

The weighting terms for the numerical fitting procedure were defined using the definition of the  $\chi^2$  distribution and a scaling factor for the covariance matrix. The latter correctly reflected the noise of the experimental data in the computed i.e. the covariance matrix will correctly estimate the confidence intervals for the fitted parameters.

Moreover, the confidence intervals were helpful for determining the number of semiconductive contributions. The estimation of the confidence intervals can be used as a break point of the iterative search when the intervals of two contributions are overlapping i.e. they are no more statistically discernable.

Experimental spectra were tested with up to 12 contributions over 3 different potentials and the estimated confidence intervals were helpfull at asserting that the semiconductive contributions are statistically discernable.



# Index

- accumulation, 10
- band
  - bending, 9
  - conduction, 7–9
  - gap, 12, 13
  - valence, 7–9
- bandgap, 7
- coefficient
  - absorption, 13
- conduction
  - electronic, 8
- conductors, 7
- depletion, 10, 13
- doping, 8
  - n-type, 8
  - p-type, 8
- Fermi
  - level, 8, 9
  - mid-gap, 8
  - position, 8
  - shift, 8
- Gärtner-Butler, 7
  - linear transform, 13
  - model, 12
- illumination, 10
- isolators, 7
- junction, 10
- mott-schottky, 13
- photocurrent, 12, 13
- photoexcitation, 8
- photovoltaic, 7
- potential
  - electrochemical, 8
  - flat band, 10, 12, 13
- Schottky, 10
- semiconductors, 7
- space charge, 9, 12, 13
- thermal excitation, 8
- transitions
  - direct, 13
  - indirect, 13